Heterogeneity and nonaffinity of cell-induced matrix displacements

Brian Burkel, Maria Proestaki, Stephen Tyznik, and Jacob Notbohm

Phys. Rev. E **98**, 052410 — Published 26 November 2018

DOI: 10.1103/PhysRevE.98.052410

Heterogeneity and nonaffinity of cell-induced matrix displacements

Brian Burkel,[1] Maria Proestaki,[1] Stephen Tyznik,[1,2] Jacob Notbohm[1,2,3]

[1] Department of Engineering Physics, University of Wisconsin-Madison
[2] Department of Mechanical Engineering, University of Wisconsin-Madison
[3] University of Wisconsin Carbone Cancer Center, Madison, WI

ABSTRACT

Cell contractile forces deform and reorganize the surrounding matrix, but the relationship between the forces and the resulting displacements is complicated by the fact that the fibrous structure brings about a complex set of mechanical properties. Many studies have quantified nonlinear and time-dependent properties at macroscopic scales, but it is unclear whether macroscopic properties apply to the scale of a cell, where the matrix is composed of a heterogeneous network of fibers. To address this question, we mimicked the contraction of a cell embedded within a fibrous collagen matrix and quantified the resulting displacements. The data revealed displacements that were heterogeneous and nonaffine. The heterogeneity was reproducible during cyclic loading, and it decreased with decreasing fiber length. Both the experiments and a fiber network model showed that the heterogeneous displacements decayed over distance at a rate no faster than the average displacement field, indicating no transition to homogeneous continuum behavior. Experiments with cells fully embedded in collagen matrices revealed the presence of heterogeneous displacements as well, exposing the dramatic heterogeneity in matrix reorganization that is induced by cells at different positions within the same fibrous matrix.

KEY WORDS

Cell mechanics, matrix, heterogeneity, fiber network, digital image correlation

I. INTRODUCTION

The mechanics of fibrous materials such as those that comprise the extracellular matrix (ECM) underpin many facets of biology. At the scale of tissues, the ECM provides mechanical support that resists forces and provides structure. At the cellular level, the ECM provides a complex set of physical cues that affect cell contraction and migration [1–5], differentiation [6,7], proliferation [4,8], and gene expression [9]. These cues often relate to mechanical forces and deformations. For example, forces applied to a cell through a substrate can affect cell contraction and the direction of migration [1,10]. In turn, cell contraction can reorganize the matrix, such as by producing aligned bands of matrix fibers [11–15], which facilitate more persistent cell migration [3,5,8]. The interplay between the localized contractile forces of a cell and the matrix displacements remains unclear, in part because our understanding of the mechanics of fibrous materials across scales remains incomplete. Numerous studies have quantified non-linear [16–19] and time-dependent properties [20–22] of fibrous ECM materials, but those studies typically considered average behavior of macroscopic specimens; how these studies apply to the microscale on which cells deform the matrix is far less clear. A key challenge at this scale is that the ECM is not a continuum but rather a heterogeneous network of fibers having lengths only slightly smaller than the size of a cell.

To characterize matrix heterogeneity at the scale of a cell, we examine how heterogeneity in the stiffness of a material affects the displacement field. Consider an affine loading, defined as one that would put a homogeneous material under uniform strain. If the material had local heterogeneities in stiffness, the resulting displacement field would deviate from the case of uniform strain, that is, the displacements would be nonaffine [23]. Therefore, for affine loading conditions, local fluctuations in stiffness can be

quantified by nonaffinity. Numerous theoretical models for fiber networks have observed nonaffine displacements [24–28] by treating each fiber as a beam that resists axial forces and bending. As the fibers are long and thin, the dimensionless ratio of stiffness in bending to stretching, κ, is typically on the order of 10^{-5} to 10^{-4} [29–32]. Deformations are therefore dominated by soft bending modes, many of which produce nonaffine or heterogeneous fiber displacements. Though studies differ in their metrics used to quantify nonaffinity and heterogeneity, experiments have established that displacements in fibrous materials are heterogeneous, by quantifying, for example, rotation of fibers [33] or displacements at points [34–36].

The magnitude of this heterogeneity on the length scale of a cell remains unclear. This is perhaps most relevant for recent endeavors to extend traction force microscopy to cells embedded within three-dimensional fibrous materials. Those studies used constitutive relationships based on continuum mechanics [37–39], which requires the matrix to be homogeneous at the length scale of the cell. Even the studies that analyzed only the displacement field assumed the displacements to be smooth when computing the strains [40–42]. Some justification for these assumptions comes from the intuition that for some loading conditions, e.g, small deformations over large length scales, the matrix should become essentially homogeneous. Consistent with intuition, a model that simulated a local point force applied to a fiber network [25] predicted that heterogeneous modes in the displacement field decayed quickly over distance, with exponential decay having a decay constant of $l_c\kappa^{-1/6}$, where l_c is the distance between fiber-to-fiber connections, and κ is the dimensionless bending stiffness. For κ on the order of 10^{-4}, this gives a decay constant of $4.6l_c$. If this is correct, any cell larger than a few fiber lengths would sense the network as being a continuum. However, a different model observed no length scale for which heterogenous displacements go to zero [27], which is consistent with a recent prediction that heterogeneous displacements decay no more quickly than average ones [28]. It is therefore unclear whether the matrix becomes essentially homogeneous at some length scale.

Here, we experimentally measured heterogeneous displacements within a network of collagen fibers. Using spherical microspheres made of an active hydrogel, poly(N-isopropylacrylamide) (PNIPAAm), we induced isotropic, microscale contraction mimicking that of a cell. The experimental data show that the heterogeneous displacements decay no more quickly than the total displacements, indicating no transition to homogeneous behavior, even for small displacements far from the contracting microsphere. Consistent with this, though heterogeneity is reduced by decreasing the fiber length, it remains nonzero for matrices having average fiber length as small as 4 μm. Cell-induced displacements are also observed to be heterogeneous, implying that at the scale of a cell, the matrix is better described as a network of fibers rather than as a continuum.

II. MATERIALS AND METHODS

A. Preparation of Samples for Imaging

PNIPAAm microspheres were made as described previously [43]. The PNIPAAm microspheres had a modulus of order 20 kPa [44], which is ~2 orders of magnitude larger than that of the collagen networks [16–19]. Therefore, compared to the collagen networks, the microspheres were essentially rigid. The PNIPAAm microspheres typically ranged in size from a few μm to more than 100 μm. For this study, we analyzed data for microspheres in the range of 50–100 μm.

The microspheres were embedded in networks of rat tail collagen I (Corning) that was fluorescently labeled with Alexa Fluor 488 (Thermo Fisher Scientific). To connect the collagen fibers to the PNIPAAm microspheres, the fibers were covalently bonded to the microspheres using sulfo-SANPAH (Proteochem). The sulfo-SANPAH (1 mg/ml, diluted in 0.05 M HEPES solution) was added to washed microspheres, and the solution was exposed to ultraviolet light of a biosafety cabinet for 10 minutes. After exposure, the sulfo-SANPAH solution was removed, and the treated PNIPAAm microspheres were washed with 0.05 M HEPES solution and 1× PBS to remove excess sulfo-SANPAH mixture. Alexa-labeled collagen was then mixed 1:20 with unlabeled acidified rat tail collagen I (Corning) and neutralized with 2× HEPES

solution as previously described [43,45]. It was diluted to its final concentration (ranging from 2.5 to 4 mg/mL) with the addition of sulfo-SANPAH treated PNIPAAm microspheres. This collagen/PNIPAAm microsphere mixture was then slowly drawn through a PDMS microfluidic channel as previously described [43,45], and maintained at 22°C, 27°C, or 30°C, with increasing polymerization temperature producing collagen networks with shorter fibers [46,47]. Upon neutralization with the 2× HEPES solution (pH 7.4), the collagen solution self-polymerized, and no crosslinking agents were added. After 1 hr, 1× PBS was added to prevent dehydration during image acquisition.

For comparison to experiments in collagen, some experiments were performed with PNIPAAm microspheres embedded in polyacrylamide composed of 3% acrylamide and 0.06% bis-acrylamide, polymerized with 0.01% ammonium persulfate and 0.05% TEMED (Biorad). 0.5 μm red fluorescent particles (FluoSpheres, Life Technologies) were embedded in the polyacrylamide to enable fluorescent imaging.

To quantify fiber lengths resulting from different polymerization temperatures, 100 μl of the Alexa-488 labeled collagen mixture was added to the bottom of a glass bottom dish (CellVis) and covered with an 18 mm circular cover glass to spread the gel uniformly. The neutralized collagen was then quickly transferred to the required temperatures and allowed to polymerize.

In experiments with cells, 4T1 cells were seeded at a density of 15,000 cells per ml and embedded in 2.5 or 3.5 mg/ml Alexa 488-labeled collagen. The cell/collagen mixture was then drawn through a PDMS microfluidic channel as previously described [45], and polymerized at either 22°C or 37°C. Cells were incubated at 37°C overnight in Dulbecco's Modified Eagle's Medium with 10% fetal bovine serum before imaging. Prior to imaging, the cells were stained with a 6.25 μg/ml solution of dye (CellTracker Red CMTPX, Thermo Fisher) for 1.5 hrs at 37°C.

B. Microscopy

Fluorescent images were collected on an Eclipse Ti microscope (Nikon) with a CSU-X confocal spinning disk (Yokogawa) and a Zyla sCMOS camera (Andor) and run by the IQ3 acquisition software (Andor). Unless stated otherwise in the text, imaging was performed with a 20× (0.75 numerical aperture) objective (Nikon), and image stacks were collected at 0.5 μm increments. As stated in the text, a 10× (0.45 numerical aperture) was used in some cases to achieve greater field of view; 10× imaging collected image stacks at 1.5 μm increments. To control contraction of the PNIPAAm microspheres, the temperature was controlled using a H301 stage top incubator with a UNO controller (Okolab). To quantify effects of changing temperature on the displacement field, we measured both total displacements (as described in section II.D.) and local nonaffine displacements (as defined in section II.G.), and observed both to be less than 0.1 μm on average (Supplemental Fig. S1 [48]). Therefore, any displacement measurement that is much larger than 0.1 μm is minimally affected by the temperature change.

Separate imaging occurred at higher resolution to measure fiber lengths. For this, fluorescent images of the collagen gels were collected on a Bruker multiphoton system with a Coherent Chameleon laser on a Nikon Eclipse Ti microscope base. The laser was tuned to 890 nm, and Prairie View 5.3 software was used to control acquisition parameters. A 40× (1.15 numerical aperture) objective (Nikon) was used to collect image stacks taken at 10 μm increments. Images were scanned at 1024 × 1024 pixels with a pixel size of 0.146 × 0.146 μm^2. The image stack was started 50 μm from the bottom surface to avoid potential effects of the bottom cover glass.

C. Quantification of Fiber Lengths

Single images from each stack of high resolution images were segmented using Seedwater Segmenter [49]. The segmentation gave areas, which corresponded to pores in the collagen network, and lines, which represented the collagen fibers. For each collagen network, we calculated the median of the pore areas for 10 different segmented images; the fiber length was then taken to be the square root. For all networks,

variability in fiber length from image to image was <2% of the estimated fiber length. Due to the finite resolution of the confocal microscope, the individual images had a thickness of about 1 μm, which resulted in unconnected fibers crossing one another in the images [50]. The segmentation detected these crossing fibers and incorrectly identified them as connections between fibers. To account for this, we manually counted the number of unconnected crossings for 10 fibers in each type of collagen network, finding the number to vary from 6.3 ± 0.9 (mean ± standard deviation) for short fibers at a collagen concentration of 4 mg/ml to 15.7 ± 1.0 for a collagen concentration of 2.5 mg/ml. The product of the segment lengths, computed from the segmented images, and the number of crossings per fiber thus gave the final estimate of average fiber length. For the 2.5 mg/ml collagen networks polymerized at 22°C and 37°C, average fiber lengths were found to be 37.0 ± 4.2 μm (mean ± standard deviation, where the standard deviations result from variability in the number of unconnected crossings per fiber) and 13.7 ± 0.9 μm, respectively. The 4 mg/ml collagen gels that were polymerized at 22°C and 30°C had average fiber lengths of 18.7 ± 3.3 μm and 4.2 ± 0.6 μm, respectively.

D. Digital Image Correlation

After imaging the collagen fibers, displacements were computed using digital image correlation (DIC). From one time point to the next, the focus changed due to drift, which we accounted for using digital volume correlation [51] to compute the focal drift and to select the image plane corresponding to the center of the PNIPAAm microsphere or cell at each time point. Images were then analyzed with DIC using Fast Iterative Digital Image Correlation (https://github.com/FranckLab/FIDIC) [51]. Subsets of 64 × 64 pixels were used with a spacing of 16 pixels. At 20× magnification, 1 pix = 0.325 μm; at 10×, 1 pix = 0.65 μm. To avoid errors in computing displacements near the boundary of each microsphere, displacements were computed only where a full subset overlapped regions of the fibrous matrix. As a result, displacements were not computed within half diagonal of a subset (i.e., within $\sqrt{2} \times 32$ pix) of the microsphere. Regions where displacements were not computed are shown in black. To correlate the large displacements, we ran the DIC incrementally and summed the results to compute the displacement with respect to the undeformed reference.

Because the contrast pattern for image correlation was the image of collagen fibers, the DIC computed erroneous values of displacement in locations where the fiber density was low. To avoid errors resulting from erroneous correlation, we eliminated points from the analysis using the following procedure. We computed the gradient of the image with the Sobel kernel using Matlab R2015a (The Mathworks) using the built-in *edge* command. A threshold was chosen; locations having a gradient greater than the threshold were identified. Those locations were then dilated by 3 grid points on each side. All displacements located in the dilated region were discarded from analysis; these locations appear as white spots in the figures.

E. Definition of Heterogeneity

As the PNIPAAm microspheres contract uniformly, continuum mechanics would predict a homogeneous material to deform in the radial direction. To evaluate heterogeneous displacements, we first defined a homogeneous solution by fitting the radial displacements to the equation

$$u_{fit} = -Ar^{-n}, \quad \text{(Eq. 1)}$$

where A and n are fitting parameters [43]. For linear elastic materials, $n = 2$, and the constant A depends on the moduli of matrix and microsphere and the contraction of the microsphere. By contrast, fibrous materials like collagen are nonlinear with $n < 2$, indicating long-range displacements that result from alignment of fibers in tension and buckling of fibers in compression [15,43,52,53]. Because the fibrous matrix is heterogeneous, displacements fluctuate over space. We thus define the heterogenous displacements $\boldsymbol{u'}$ to be the deviation from average behavior:

$$\boldsymbol{u'} = \boldsymbol{u} - \boldsymbol{u}_{fit}, \quad \text{(Eq. 2)}$$

where $\boldsymbol{u}$ is the experimentally measured displacement field and $\boldsymbol{u_{fit}} = -u_{fit}\,\boldsymbol{e_r}$ with scalar u_{fit} given by Eq. 1 and vector $\boldsymbol{e_r}$ being the unit vector in the radial direction with outward defined as positive. Note that the negative sign in the definition for $\boldsymbol{u_{fit}}$ cancels the negative sign in Eq. 1.

F. Autocorrelation of Displacement Field

An autocorrelation of the heterogeneous displacement field $\boldsymbol{u'}$ was used to compute the typical size of a heterogeneous region. The autocorrelation followed the standard equation for autocorrelation of a vector field,

$$C(X,Y) = \frac{1}{Ns^2}\sum_x \sum_y \overline{\boldsymbol{u'}}(x,y) \cdot \overline{\boldsymbol{u'}}(x-X, y-Y), \qquad \text{(Eq. 3)}$$

where $\overline{\boldsymbol{u'}} = \boldsymbol{u'} - \boldsymbol{u'_m}$ and $\boldsymbol{u'_m}$ is the mean of the heterogeneous displacement field $\boldsymbol{u'}$. The factor $1/Ns^2$, with N equal to the number of data points and s^2 equal to the variance of $\boldsymbol{u'}$, gives a normalization such that the maximum value of C is $C(0,0) = 1$. In this notation, bold symbols represent vectors, and the dot $(\cdot)$ represents a dot product. Lower case x and y are spatial coordinates, and upper case X and Y are coordinates in the autocorrelation space.

G. Definition of Local Nonaffinity

In experiments with cells, we used a second definition of heterogeneity, called local nonaffinity. We began by choosing a 47×47 μm^2 region of interest. (Justification for this size of region is given in section III.C.) In-plane displacement components within the region of interest u and v were fit to the equations $u = a_1 + b_1x + c_1y$ and $v = a_2 + b_2x + c_2y$. As each of these functions were linear, they defined an affine displacement field in the region of interest. Deviations from the fitted affine displacements resulted from local heterogeneities in the displacement field. We therefore defined a second metric for heterogeneity by computing the difference between the actual displacement at the center of the region of interest and the affine displacement. We called the difference the local nonaffinity. This process was repeated for many regions of interest to give full-field data on local nonaffinity.

H. Fiber Network Model

Two different methods were used to generate random fiber networks for theoretical modeling. The first is commonly used to mimic networks of intracellular fibers such as actin [24]. This method deposited fibers of a chosen length at random orientations and positions. All overlapping fibers were connected. This network is characterized by two length scales, the total fiber length l_t and the average length between connections, l_c. Here we used fibers having a ratio $l_t / l_c = 25$, which is in the middle of the range used in previous studies [24,25]. This produced networks with an average connectivity, defined as the number of fibers meeting at each node, of 3.8. The second method for generating the fiber network has been proposed to match the structure of extracellular matrix fibers such as fibrin and collagen [28,54,55]. Full details are described by Grimmer et al [28]. First, nodes were randomly seeded in the domain and a value of connectivity was given to each node. Next, fibers were randomly connected between nodes until each node's connectivity was reached. After this procedure, the average connectivity of each network was found to be 3.3, which is close to the experimentally-measured value of 3.4 [54,55]. The network then underwent a simulated annealing process that matched the average fiber length to a desired mean fiber length L. Finally, the nodes were moved so that the fibers at each connection met with angles that more closely resembled the connections in networks of collagen fibers. As this the second type of model connected nodes rather than fibers, approximately half of the locations that fibers crossed were unconnected in this type of network. This is consistent with our observation of unconnected crossing fibers described in section II.C. To compare the actin and collagen network models, l_c in the first model and L in the second model were set to be equal. For simplicity, we will call this length L for the rest of

this manuscript. In the experiments, values for L in a collagen network range from 4 to 37 μm, as described in section II.C.

The domain simulated was an annulus with inner and outer radii of $5L$ and $100L$. Though the model is two-dimensional, previous studies have shown that general trends match between two-dimensional and three-dimensional models [30,31,56], which allows us to compare qualitative trends observed in the model to those observed in the three-dimensional experiments. Five different networks of each type were generated. Nodes on the outer boundary were constrained to have no translation or rotation. Nodes with a radial position between $5L$ and $6L$ were displaced radially by 1% of the annulus' inner radius and constricted not to rotate. This range of radial positions produced a uniform contraction along the inner boundary of the annulus. The fibers were modeled as linear two-node Timoshenko beam elements and connections were tied, which fully coupled displacement and rotation between the fibers. The bending stiffness k_b and axial stiffness k_a of the fibers were combined into a single dimensionless ratio κ given by $\kappa = k_b/(k_a L^2)$. Previous studies have reported that the value of dimensionless bending stiffness κ for collagen fibers is $\sim 10^{-4}$ [29–32], which was also used here. The model was implemented in the finite element software Abaqus 6.12 (Dassault Systemes). The system was solved using the software's implicit static solver. The radial displacements from the simulation were then fit to the equation

$$u_{fit} = -(Ar^n + Br^{-n}), \qquad \text{(Eq. 4)}$$

which is similar to Eq. 1 but with an added second term, which is necessary when using a fixed outer boundary [28]. This equation was then used with Eq. 2 to compute the heterogeneous displacements $\boldsymbol{u'}$. To avoid artifacts from the fixed outer boundary, data are reported for nodes inside 70% of the outer radius.

I. Statistical Analysis

Comparisons between groups used medians so that the results would be insensitive to locations having erroneous displacements. Statistical analysis was performed in Matlab R2015a using the rank sum test or, for multiple comparisons, the Krushkal-Wallis test, both of which are nonparametric.

III. RESULTS

A. Heterogeneous Displacements

To induce contractile displacement fields on the length scale of a cell, we embedded microspheres of PNIPAAm within a matrix of collagen I fibers [43]. Upon heating, the microspheres contracted, and we computed the resulting field of displacements using DIC (Fig. 1). Because the random contrast pattern used for DIC was the network of fibers itself, the DIC sometimes failed to determine displacements in regions of low fiber density. To identify these erroneous locations, we used a threshold based on the gradient of the displacement field as described in the Methods. Whereas many image correlation algorithms use interpolation to fill in erroneous regions, we show them here in white and leave them out of the following analyses. The equivalent of Fig. 1 with no erroneous data points removed is given in Supplemental Fig. S2.

The data show nonzero displacements in the angular (θ) direction (Fig. 1e). As the microsphere contracts uniformly, applying only radial displacements at its boundaries, the θ displacements result from local variations in stiffness of the fiber network. Heterogeneity is also present in the field of radial displacements, as indicated by the fluctuations over space (Fig. 1d). The heterogeneous displacements $\boldsymbol{u'}$ as defined by Eq. 1 are large (Fig. 1g), with maximum magnitude approximately half that of the measured displacements (Fig. 1c).

To demonstrate that the heterogeneity was not simply a result of experimental noise, we imaged a PNIPAAm microsphere during three cycles of contraction. Before inducing contraction, we acquired an image of the reference state. We then induced a cycle of contraction that increased the temperature twice, generating states of low and high contraction, followed by recovery of the microsphere to its initial size.

This cycle of low contraction–high contraction–recovery was carried out thrice; displacements were computed for the low contraction and recovered time points (Fig. 2). At the low contraction time point, displacements in the first cycle were smaller than in later cycles (Fig. 2b). Additionally, there were noticeable permanent displacements after the first loading cycle (Fig. 2c). These observations are consistent with studies that applied multiple cycles of uniform shear and observed permanent deformations after the first loading cycle [18,21]. The permanent displacements have been shown to result from preconditioning of the fiber network caused by fibers reorienting or increasing in length in directions of tension [21]. Strikingly, after the preconditioning of the first cycle, the displacements—both $\boldsymbol{u}$ and $\boldsymbol{u'}$—appeared nearly identical (Fig 2b,c), indicating that the heterogenous displacements observed here are not due to random noise but rather result from repeatable local displacements within the network. To compare displacements at different cycles, we computed the normalized difference D in displacement between cycles according to the equation

$$D = \left[\left\langle (u_m - u_n)^2 \right\rangle \Big/ \left\langle (u_m + u_n)^2 \right\rangle \right]^{1/2}, \qquad \text{(Eq. 5)}$$

where u is the magnitude of the displacement, subscripts indicate cycles m and n (m, n = 1, 2, or 3), and the angled brackets $\langle\ \rangle$ indicate a mean over all locations in the image. Numerous microspheres were then subjected to the same cycles of contraction and recovery illustrated in Fig. 2a. The normalized difference D was computed for each microsphere for both the total displacement field (Fig. 2d) and the heterogeneous displacement field (Fig. 2e). On average, total displacements of cycles 2 and 3 differed by only 3%, and heterogeneous displacements differed by only 10%. As these differences between cycles are so small, we conclude that experimental noise had a negligible effect on the results.

As the measurement of displacements is robust, we now consider how heterogeneity is affected by fiber length, which has been considered in previous studies [24,25,27,28,35]. We modulated the fiber length while keeping the overall protein concentration the same (4 mg/ml) by polymerizing mixtures of the same collagen concentration at 22°C (to generate longer fibers with average length 18.7 μm) or 30°C (to generate shorter fibers with average length 4.2 μm). We used a dimensionless metric for heterogeneity, $\chi = u' / u$, where χ was computed and averaged over all positions in each of the networks studied. As we will demonstrate in the next section this is a rigorous means to quantify the heterogeneity. Fiber networks having short fibers had lower dimensionless heterogeneity χ than those with long fibers (Fig. 3). Additionally, heterogeneity of networks with short fibers was not statistically different from polyacrylamide (Fig. 3), which is heterogeneous at small length scales [57,58]. For example, polyacrylamide made with the same concentration of acrylamide and bisacrylamide used here was tested with nanoindentation and found to have a mean Young's modulus of 0.48 kPa with a standard deviation of 0.16 kPa [59]. Assuming a normal distribution, the modulus would therefore vary by a factor of >5. This is consistent with a different study that reported the shear modulus of polyacrylamide to vary by a factor of ~7 [57]. For the polyacrylamide used here, the pore size is ≈330 nm [60]. At larger length scales, such as the 4.2 μm collagen fibers, heterogeneity in the local stiffness may be lower than the factor of 5-7, but it is nonetheless significant as demonstrated by the nonzero values of χ.

B. Decay of Heterogeneity Over Distance

An interesting observation is that the heterogeneous displacements are not always largest near the contracting microsphere—they sometimes have large magnitudes at distances of several tens of microns from the microsphere (e.g., Fig. 1g, arrow head). Intuitively one may expect that at sufficiently small displacements, the network should behave as a homogeneous continuum. This would imply that the regions of large heterogeneity as shown by the arrow head in Fig. 1g would occur only near the microsphere, where deformations are largest. For heterogeneous displacements to become negligible at small displacements, they would have to decay more quickly over distance than total displacements. This hypothesis is consistent with a previous theoretical model that predicted heterogeneous displacements to

decay exponentially over distance [25], which is faster than the power law decay of total displacements observed in our experiments.

To determine whether the network becomes essentially homogeneous at small deformations, we used a theoretical model for a fiber network that simulates stretching, bending, and buckling of each fiber. Two different fiber networks were simulated. The first, typically used to simulate intracellular networks such as actin [24], deposited fibers randomly and connected the ones that crossed. The second, designed to match fibrous extracellular materials like collagen, deposited nodes, connected them with fibers, and moved the nodes to achieve a desired distribution of fiber lengths [28,54,55]. Representative images of a collagen network and the two simulated fiber networks are given in Fig. 4a-c. For both simulated networks, a contracting circle of initial radius 5 fiber lengths contracted by 1% within a network having radius of 100 fiber lengths. The heterogeneous displacements $\boldsymbol{u}'$ were computed and their magnitudes were averaged around the circle to give heterogeneity over distance. The data are plotted on log-log and log-linear axes to compare power law and exponential fits (Fig. 4d-g). In agreement with a previous model [25] the first type of fiber network appears more linear on log-linear axes (Fig. 4d, correlation coefficient $R^2 = 0.988$) than log-log axes (Fig. 4e, $R^2 = 0.950$). By contrast, the second type appears more linear on log-log axes (Fig. 4g, $R^2 = 0.988$) than log-linear (Fig. 4f, $R^2 = 0.957$). These differences are small though, and for either model, the heterogeneous displacements fit to Eq. 4 with an exponent n that is not statistically different from the value of n computed by fitting the total displacements. This may imply that heterogeneous displacements decay over distance at the same rate as total displacements.

The two networks can be compared further by taking the ratio of heterogeneous and total displacements, to give dimensionless heterogeneity χ. Whereas χ initially increases for the fiber network made to match actin (Fig. 4h), it remains constant for the network made to match collagen (Fig. 4i). This observation agrees with the notion that in actin networks heterogeneous displacements may initially decay exponentially (Fig. 4d and ref. [25]), but in collagen networks, heterogeneous displacements decay at the same rate as total displacements. Therefore, in collagen χ gives a useful and rigorous dimensionless metric for heterogeneity, which supports the use of χ to analyze the experimental data in Fig. 3. Furthermore, the fact that the heterogeneous displacements decay at the same rate as total displacements implies that there is no transition to homogeneous continuum behavior at small deformations far from the contracting microsphere.

To test the predicted scaling of heterogeneous displacements over distance, we performed experiments using a lower magnification (10×) objective, thereby achieving a larger field of view and data at larger distances from each contracting microsphere (Fig. 5a,b). Heterogeneous displacements for multiple microspheres are plotted against distance r from the center of each microsphere on both log-log (Fig. 5c) and log-linear (Fig. 5d) axes. For all data, the curves appear more linear on the log-log axes (Fig. 5c); at no point do the data appear linear on log-linear axes (Fig. 5d). Furthermore, the slopes of linear fits to the data on log-log axes were not statistically different for heterogeneous displacements as compared to total displacements, in agreement with predictions of the theoretical model. To determine whether the observed power law scaling was an artifact resulting from the fact that our definition of heterogeneous displacements (Eq. 2) depends on a power law fit to the radial displacements (Eq. 1), we repeated this analysis for only the angular component of displacement u_θ. It should be noted that for the axially symmetric contraction imposed here, u_θ is a heterogeneous mode of displacement, but it misses heterogeneity in the radial direction. Nevertheless, analyzing u_θ offers the advantage that it does not rely on the fitting of Eq. 1. In analyzing u_θ, we observed the same trend, with a power law better matching the decay of displacements than an exponential function (Supplemental Fig. S3). Therefore, heterogeneous displacements decay as a power law at a rate no faster than total displacements.

C. Cell-Induced Heterogeneity

The definition of heterogeneity (Eq. 2) used the fitting of Eq. 1, which applies only for the case of spherically symmetric contraction or expansion. Quantifying heterogeneity for general loading conditions, such as forces due to a contracting cell, requires a different metric for heterogeneity. The heterogeneous

displacements appear to occur within discrete regions of the same size in each image. It is therefore reasonable to establish a second metric for heterogeneity using a local region of size approximately equal to the size of a heterogeneous region. We began by quantifying the size of a heterogeneous region by performing an autocorrelation on the heterogeneous displacement data (Eq. 3 and Fig. 6a,b). To quantify the size, we define the radius $R_{1/2}$ to be the distance over which the autocorrelation declines to a value of 1/2. The typical size of a heterogeneous region is then $2R_{1/2}$, which has an average value of 42 μm (Fig. 6c). Conveniently, the value of 42 μm is approximately equal to the size of a cell, indicating that quantifying heterogeneity over a region of this size will also quantify heterogeneity at the scale of a cell.

We then considered displacement data within a 47×47 μm^2 square region of interest and computed the local nonaffinity as described in the methods. As this metric computes the deviation from a locally affine displacement, we refer to it as the local nonaffinity (Fig. 6d). To establish that this definition of local nonaffinity is meaningful, we compared it to our previous observations of heterogeneity, observing that the local nonaffine displacements fit to a power law and depend on fiber length (Supplemental Fig. S4). As these trends match those already presented, the local nonaffinity is a useful metric for heterogeneity. It offers the advantage that no fitted solution such as that in Eq. 1 is required, and thus it can be applied to any loading conditions, even those due to a contracting cell.

To investigate heterogeneous displacements resulting from the forces of cell contraction, we computed local nonaffinity of the displacement fields produced by migrating cells embedded in collagen matrices (Fig. 7). Similar to experiments with the contractile isotropic PNIPAAm microspheres, cell-induced displacements in collagen matrices made of short fibers were less heterogeneous than displacements in matrices of long fibers (Fig. 7e). This trend was observed for multiple collagen concentrations (2.5 mg/mL, Fig. 7; 3.5 mg/mL, Supplemental Fig. S5). Notably, compared to PNIPAAm microspheres, cells applied anisotropic forces along the axis of the cell, thereby magnifying the consequences of matrix heterogeneity. Whereas the isotropic forces induced by contractile PNIPAAm microspheres deformed fibers primarily in the radial direction, the anisotropic loads exerted by cells concentrated forces to a limited number of fibers oriented along the axis of the cell. With fewer fibers under tension, the directions of cell-induced displacements in longer fiber networks were more random and can be seen branching and propagating perpendicularly from the axis of cell contraction. This observation was not present in more homogeneous, shorter fiber networks wherein displacements were smooth and aligned with the axis of the cell (Fig. 7).

IV. DISCUSSION

The extracellular matrix is known for its complex mechanical cues that result in part from its heterogeneous fibrous structure. Here we mimicked the contractile forces of a cell, quantifying both heterogeneity and local nonaffinity of the resulting displacement field. Heterogeneous displacements were reproducible and significantly affected by fiber length, with more heterogeneity observed in matrices with longer fibers. Heterogeneous displacements decayed no more quickly than the total displacements, indicating no transition to homogeneous behavior. Heterogeneity in displacements induced by isolated cells migrating through a 3D matrix matched the findings from the acellular experiments with PNIPAAm microspheres. Additionally, under local anisotropic loads produced by a cell, the heterogeneous matrix structure takes on increasing importance: instead of aligning with the axis of the migrating cell, the vector field of displacements was observed to point in seemingly random directions. Importantly, these observations of heterogeneity represent the scale at which continuum behavior breaks down and contributions from individual fibers dominate.

Our experiments highlight a subtle but important difference between networks of collagen and other fibrous materials such as actin. Whereas in collagen, decreasing the fiber length made the displacement field more homogeneous (Fig. 3), experiments in actin under uniform shear observed that decreasing the fiber length made the displacements less homogeneous [35]. This difference is likely to be caused by the different structures of actin and collagen networks. In actin networks, the fibers have two characteristic lengths, the total length of the fiber L and the length between fiber connections l_c. But collagen fibers

appear to connect only at their endpoints, so for collagen $L = l_c$. As the key length for fiber bending is the distance between connections, the fiber length in collagen should be compared not to the total length of an actin fiber but rather to the distance between connections l_c. Theoretical models matching the structure of actin networks have demonstrated that reducing l_c makes the displacements more homogeneous [24,25,27], in agreement with our data.

Previous models have studied the effect of length scale on heterogeneity by averaging heterogeneous displacements over a region of some characteristic size and observing a decrease in the resulting average as the region size is increased [24,27]. We note, however, that in our experiments displacements decay with distance, so averaging over different region sizes is inappropriate. Instead, we can study how the heterogeneous displacements decay with distance from the center of the microsphere (Fig. 5, Supplemental Fig. S3). The power law decay that we observe is slower than predicted by a previous model [25], which predicted that heterogeneous displacements due to local forces decay exponentially over distance. Our modeling suggests that this difference is due to the network geometry simulated. Whereas fiber networks designed to match fibrous actin show exponential decay, networks designed to match fibrous collagen exhibit power law decay (Fig. 4). The power law decay is also present in the experimental data (Fig. 5, Supplemental Fig. S3), and it is consistent with a theoretical model that showed nonaffine displacements averaged over a region decay as a power law with increasing size of that region [27]. The power law is also consistent with the fact that fluctuations in local stiffness are correlated over space following a power law [61]. The power law scalings indicate that there is no length scale for which the fiber network becomes homogeneous, even for small deformations far from the applied loading.

That displacements are heterogeneous at all scales implies that strains defined based on the displacement gradient poorly characterize the displacement field. This has implications for efforts to quantify 3D tractions applied by cells embedded in fibrous materials. Some of those studies have inferred tractions by computing the strains [40–42], whereas others have also applied a constitutive relationship to compute tractions or energy exerted by the cell [37–39]. In principle, the power law scaling of heterogeneous displacements forbids either of these methods, though in practice the heterogeneity may be smaller than the experimental noise, in which case errors due to heterogeneity would be insignificant. A reasonable maximum level of heterogeneity may be that of polyacrylamide, which is often used for studies in cell mechanobiology. The polyacrylamide used in this study has a dimensionless heterogeneity of $\chi \approx 0.1$ (Fig. 3). To achieve values of heterogeneity this small in a collagen network, the fibers must be relatively short (e.g., 4 μm, Fig. 3). In many of the previous studies, this appears to be the case, though quantitative justification was lacking. The local nonaffinity presented here gives a quantitative means to verify that the heterogeneity is negligible.

A premise underlying this work is that the heterogeneous displacements result from local gradients in the stiffness of the fibrous network [23]. Other experiments have quantified local stiffness using active microrheology, observing stiffness to vary over space by an order of magnitude [62–65]. Similarly, an order of magnitude variation was observed in tractions at the interface between a fibrous network and a homogeneous polyacrylamide gel [66]. The variation in stiffness decreases with decreasing fiber length [65], in agreement with our data (Fig. 3). Our results are therefore consistent with data quantifying local stiffness of fibrous materials, but heterogeneous displacements should not be interpreted only through their effect on stiffness. As heterogeneity is a characteristic of the displacement field, it may offer insights for cases in which cell-induced displacement fields affect cell response to matrix mechanics. For example, cell-induced displacements propagate over a long range in fibrous materials, which may be a mechanism for long-range mechanical sensing [15,52,53]. As another example, fiber displacements are required to generate aligned bundles of fibers that direct cell migration [3,5]. As both of these examples depend on the displacements of the fibers, heterogeneity of the displacement field is likely to play an important role.

Matrix heterogeneity could produce variability in numerous cellular processes, adding to the already large set of factors causing biological variability. Recently, advanced profiling techniques like quantitative single-cell RNA sequencing have detected transcription of individual cells [67–70], observing the transcriptome to vary dramatically from one cell to the next. Chemical gradients and the availability of ligands almost certainly contribute greatly to this variability. Likewise, mechanical signals

such as stiffness also affect expression profiles [6,9]. It is often assumed, however, that in fibrous networks, the mechanical environment is homogenous at the scale of an individual cell. But the displacements are heterogeneous as well, implicating mechanics as another source of biological variability. To the cell, this heterogeneity could manifest itself as changes in stiffness that vary dramatically over space, as has been predicted by recent theoretical models [42,71]. The cell would sense the matrix not as a uniform environment, but rather as a heterogeneous one composed of numerous stiff and compliant islands. The fibrous structure could further amplify that heterogeneity by bending cell-induced displacement fields towards or away from those islands.

The heterogeneity observed here poses two interesting questions. Firstly, how does a cell sense stiffness in a heterogeneous mechanical environment? One study proposed that the cell may compensate by elongating to sample several locations simultaneously [71]. Alternatively, the cell could average measurements over time, thereby tempering its response to spatial fluctuations. Secondly, how do mechanical cues propagate through heterogeneous fibrous matrices? On two dimensional substrates, cells migrate toward stiffer environments and toward tensile mechanical forces [1], but in heterogeneous matrices, cell sensing is subject to the stochastic organization of the fibers. Voids or inclusions lying immediately in front of the migrating cell may be mechanically amplified or cloaked due to random features of the matrix. This poses the interesting idea that heterogeneity in cell sensing may not be driven totally by heterogeneity in the forces produced cell; rather, random features of the matrix and their local mechanics may predetermine the cell's response. It remains to be determined whether such matrix features can be used to control cell behavior in tissue engineering and treatments to disease.

ACKNOWLEDGMENTS

We acknowledge the Materials Science Center at the University of Wisconsin-Madison for use of the confocal microscope. This work was supported in part by National Science Foundation grant number CMMI-1749400 and by NIH NCI P30CA014520—UW Comprehensive Cancer Center Support Grant.

FIGURES

Figure 1

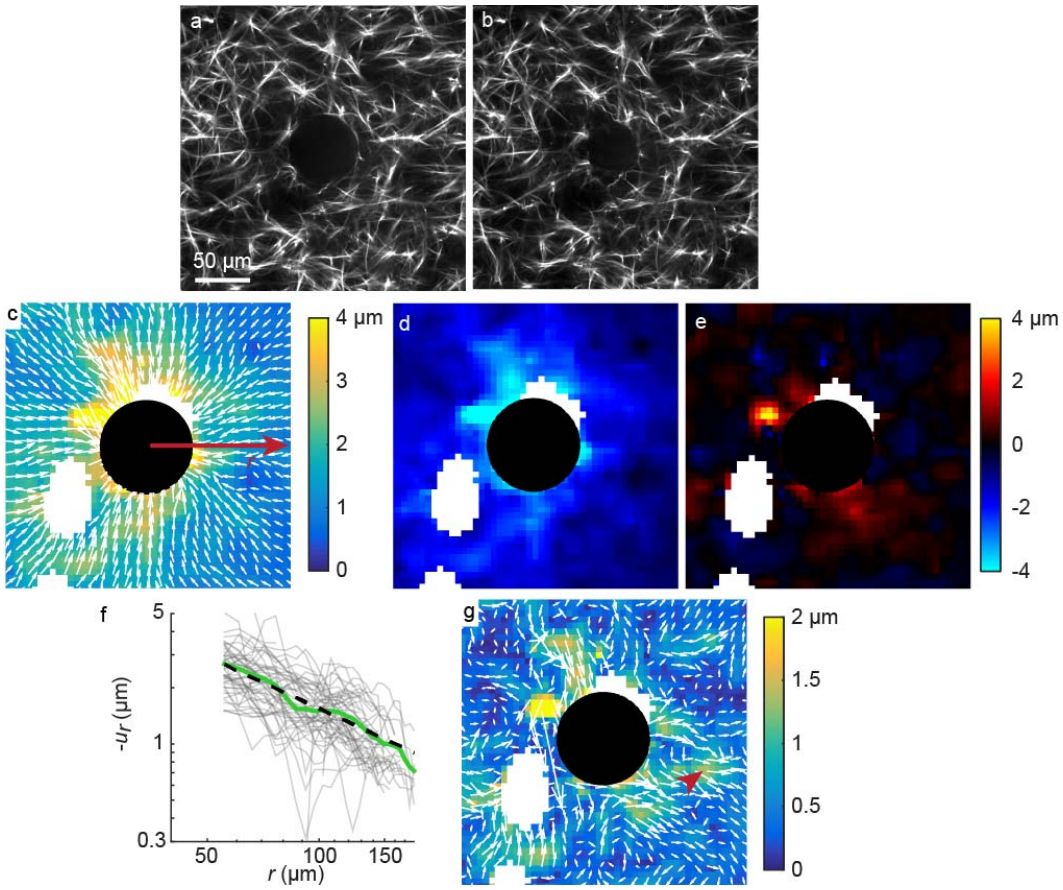

Heterogeneous displacements. (a, b) Images of collagen network (4 mg/ml, polymerized at 22°C, average fiber length 18.7 μm) before (a) and after (b) contraction of the PNIPAAm microsphere. (c) Resulting displacement field. Arrows indicate direction; colors, magnitude of displacements. (d) Radial displacements u_r with blue (negative) indicating inward. (e) Azimuthal displacements u_θ with positive being counterclockwise. (f) Paths (e.g., red arrow in panel c) are drawn outward from the center of the microsphere, and displacements are computed along those paths. The opposite of the radial displacement, $-u_r$, over distance, r, is shown for multiple paths (gray lines). The mean (solid green line) fits to Eq. 1, $u_{fit} = -Ar^{-n}$, (dashed line), which gives the fitted average displacement field. For this microsphere, $n = 0.93$. (g) The heterogeneous displacement field $\boldsymbol{u'}$, as defined by Eq. 2. In panels (c), (d), (e), and (g), white spots indicate regions that were not included in the analysis.

Figure 2

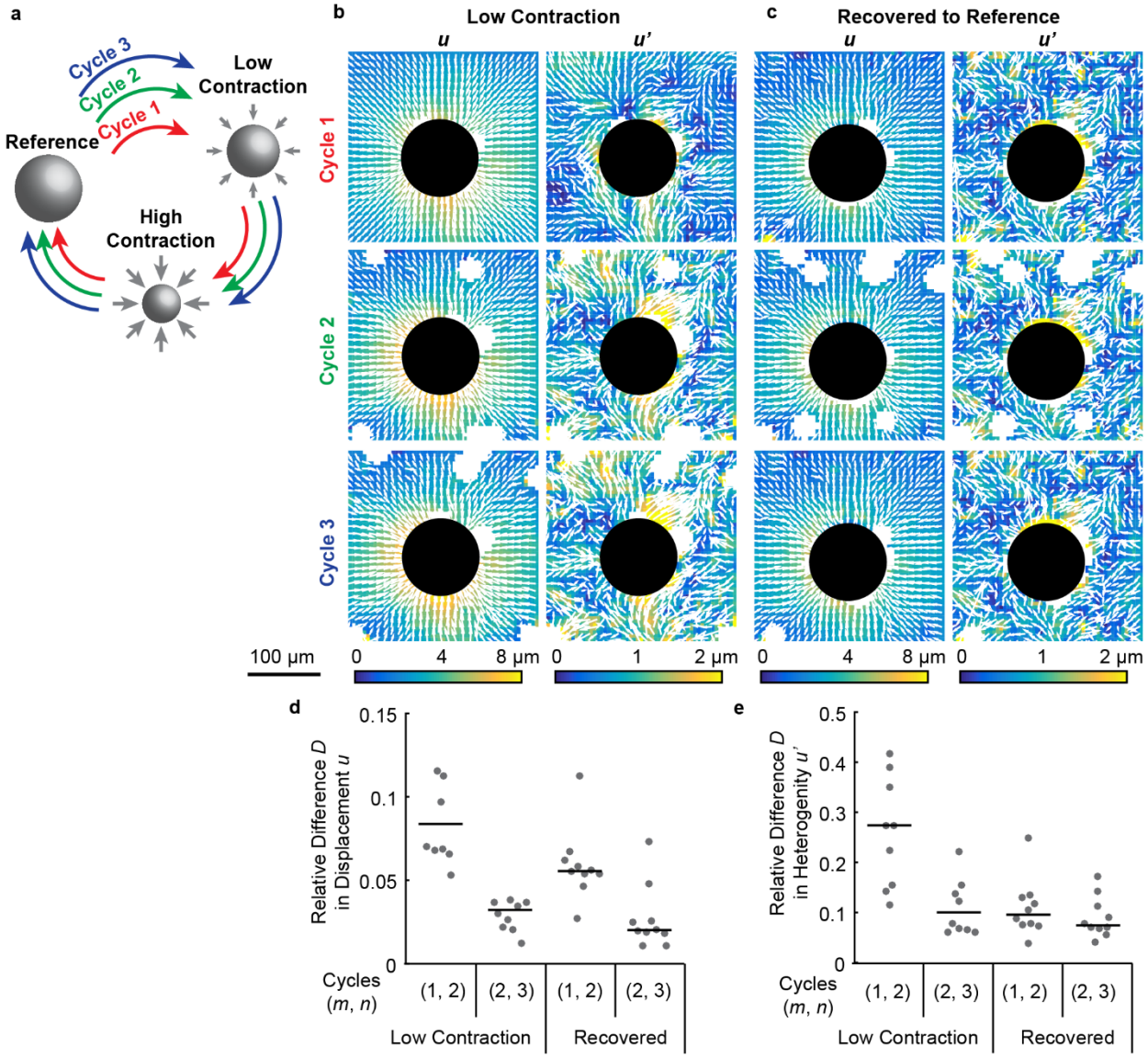

Heterogeneous displacements are reproducible during cyclic loading. (a) PNIPAAm microspheres in a collagen network (3 mg/ml, polymerized at 27°C) are imaged at a reference temperature (27°C) and then repeatedly heated to different temperatures to yield reproducible contraction. Microspheres heated to 34°C decrease in volume to yield low levels of contraction; subsequent heating to 38°C yields high levels of contraction. The microspheres are then cooled to the initial reference temperature, allowing them to recover to their initial size. Each cycle of low contraction–high contraction–recovery is repeated three times. (b, c) Total displacements ***u*** and heterogeneous displacements ***u'*** for each of three cycles at low contraction (b) or after the PNIPAAm microsphere has recovered to its initial size (c). In all cases, the reference used for DIC is the first time point acquired at 27°C. Arrows indicate direction; colors, magnitude of displacements. (d, e) Relative difference D (Eq. 5) between cycles m and n for total displacements (d) and heterogeneous displacements (e). Each dot represents an independent measurement from a separate PNIPAAm microsphere.

Figure 3

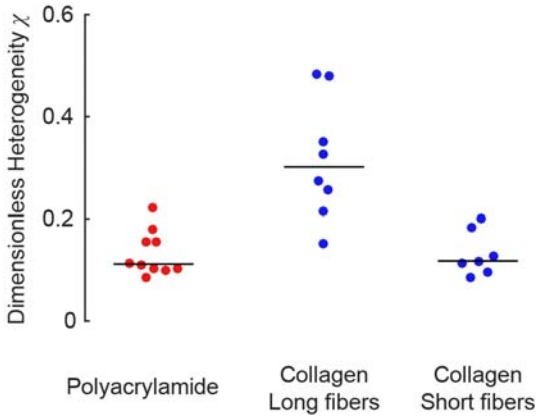

Effect of fiber length on dimensionless heterogeneity χ. Collagen matrices (4 mg/ml) having long fibers (polymerized at 22°C, average length 18.7 μm) have statistically different χ from equivalent matrices with short fibers (polymerized at 30°C, average length 4.2 μm) or polyacrylamide ($p < 0.05$, Krushkal-Wallis test with Bonferroni correction for multiple comparisons). Each dot shows the median of χ for a different microsphere. Lines show medians over all microspheres.

Figure 4

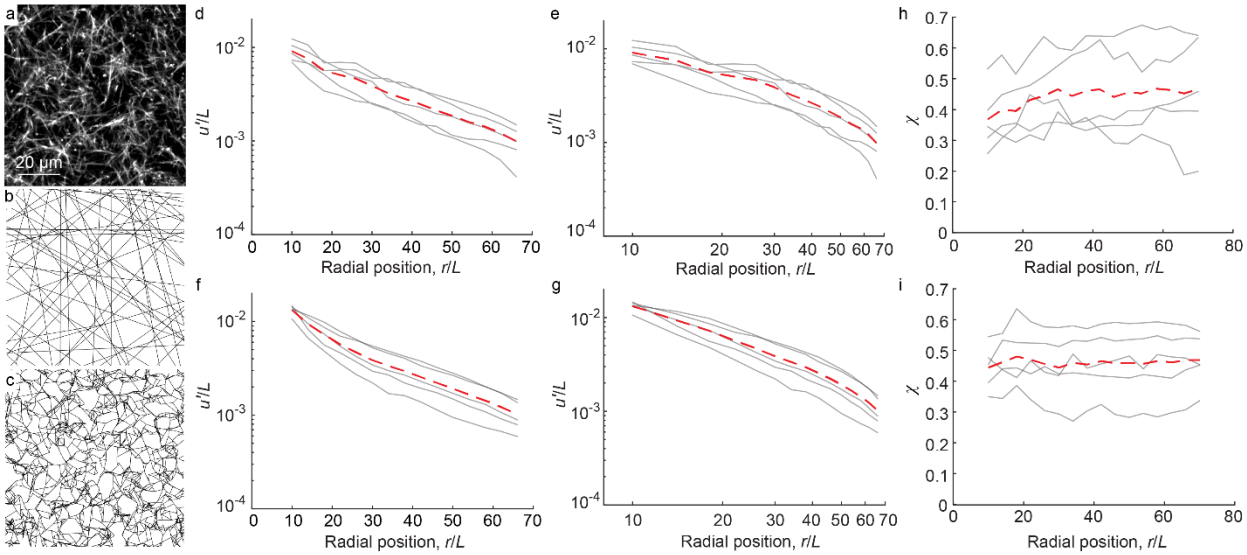

Heterogeneous displacements due to a contracting inclusion predicted by the fiber network model. (a) Representative image of collagen fiber network. (b) Representative image of first type of network, designed to match the structure of actin. In this type of network, all fibers that cross are connected. (c) Representative image of second type of network, designed to match the structure of collagen. In this type of network, approximately half of the fibers that cross are unconnected. (d-g) Decay of magnitude of heterogeneous displacement *u'* over distance for fiber networks matching the structure of actin (d, e) or collagen (f, g). Panels (d) and (f) plot the data on log-linear axes; panels (e) and (g) plot the data on log-log axes. (h, i) Dimensionless heterogeneity χ for fiber networks matching actin (h) and collagen (i). For all plots, solid lines show results a different random network; dashed lines indicate the means over all networks.

Figure 5

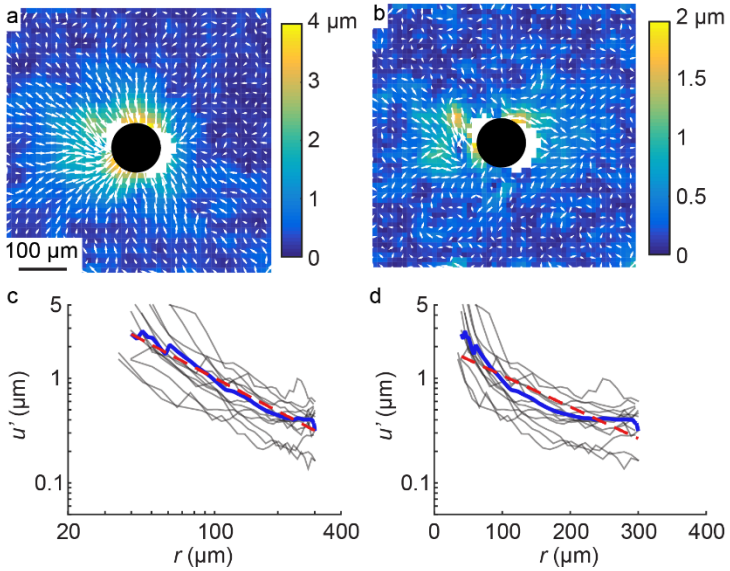

Heterogeneous displacements decay as power law. (a, b) Representative field of total displacements $\boldsymbol{u}$ (a) and heterogeneous displacements $\boldsymbol{u'}$ (b) in fibrous collagen matrices (4 mg/ml, polymerized at 22°C, average fiber length 18.7 μm). Arrows indicate direction; colors, magnitude of displacements. (c, d) As in Fig. 1f, heterogeneous displacements are determined along radial paths drawn outward from the center of each microsphere and averaged along these paths. Each gray line shows average of heterogeneous displacements for a single microsphere; blue lines show the average over all microspheres. Axes are log-log (c) and log-linear (d). Dashed red lines are linear on each of the axes, corresponding to fits to a power law and an exponential, respectively.

Figure 6

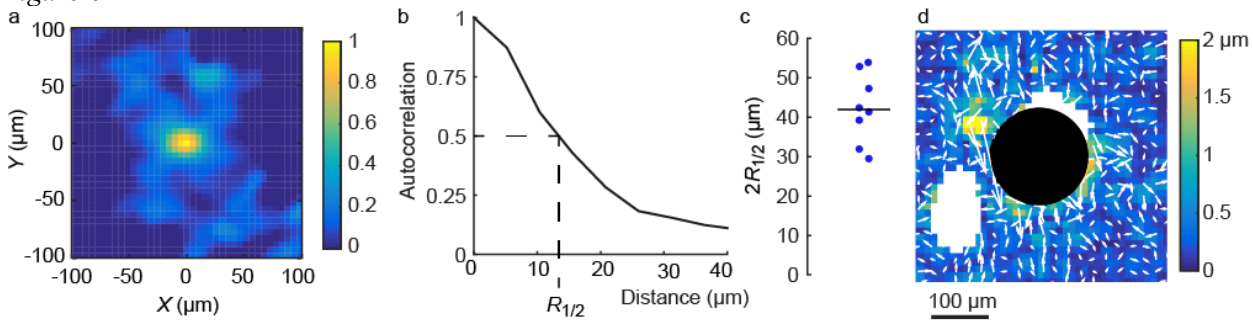

Measurement of local nonaffinity. (a) Autocorrelation of heterogeneous displacement field in Fig. 1g. (b) The autocorrelation is averaged around angle by drawing circles centered at the origin of panel a and taking the average around each circle, giving autocorrelation versus distance. The distance $R_{1/2}$ for which the autocorrelation drops to a value of 1/2 is a characteristic radius of a region of heterogeneous displacement. (c) The size of a heterogeneous region $R_{1/2}$ is computed for multiple different collagen networks (all 4 mg/mL, polymerized at 22°C) having long fibers (average length 18.7 μm). Each dot represents a different network; line represents median of 42 μm. (d) Local nonaffinity, which is defined as the difference between the measured displacement $\boldsymbol{u}$ and an affine fitted one $\boldsymbol{u}_{aff}$. For each position in

space, $\boldsymbol{u}_{aff}$ is computed by fitting all displacements in a 47×47 μm^2 window around that point to a plane of the form $u = a + bx + cy$. The fitting is performed for both components of the displacement vector.

Figure 7

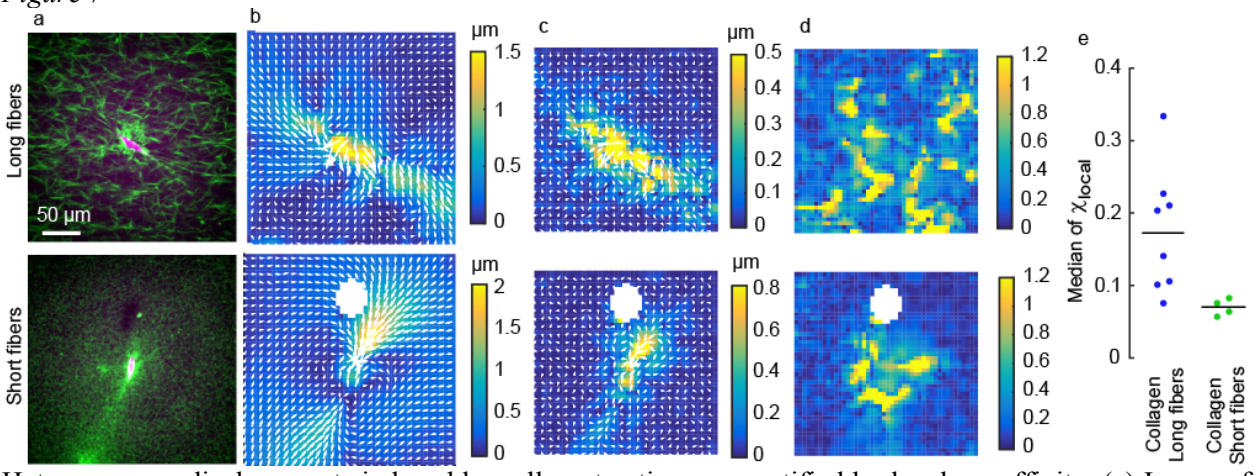

Heterogeneous displacements induced by cell contraction as quantified by local nonaffinity. (a) Image of single cell (magenta) embedded in 2.5 mg/mL collagen network (green) with either long fibers (polymerized at 22°C, average length 37.0 μm) or short fibers (polymerized at 37°C, average length 13.7 μm). (b) Cell-induced displacement field showing magnitude (colors) and direction (quivers). (c) Local nonaffine displacement. (d) Dimensionless local nonaffinity χ_{local}. (e) Comparison of median dimensionless local nonaffinity for networks having short or long fibers. Each dot represents median of local nonaffine displacements due to a different cell; lines represent the medians. The two data sets are statistically different ($p < 0.01$, rank sum statistical test).

REFERENCES

[1] C.-M. Lo, H.-B. Wang, M. Dembo, and Y. Wang, Cell Movement Is Guided by the Rigidity of the Substrate, Biophys. J. **79**, 144 (2000).

[2] M. J. Paszek, N. Zahir, K. R. Johnson, J. N. Lakins, G. I. Rozenberg, A. Gefen, C. A. Reinhart-King, S. S. Margulies, M. Dembo, D. Boettiger, D. A. Hammer, and V. M. Weaver, Tensional Homeostasis and the Malignant Phenotype, Cancer Cell **8**, 241 (2005).

[3] P. P. Provenzano, D. R. Inman, K. W. Eliceiri, S. M. Trier, and P. J. Keely, Contact Guidance Mediated Three-Dimensional Cell Migration Is Regulated by Rho/ROCK-Dependent Matrix Reorganization, Biophys. J. **95**, 5374 (2008).

[4] T. A. Ulrich, E. M. de J. Pardo, and S. Kumar, The Mechanical Rigidity of the Extracellular Matrix Regulates the Structure, Motility, and Proliferation of Glioma Cells, Cancer Res. **69**, 4167 (2009).

[5] K. M. Riching, B. L. Cox, M. R. Salick, C. Pehlke, A. S. Riching, S. M. Ponik, B. R. Bass, W. C. Crone, Y. Jiang, A. M. Weaver, K. W. Eliceiri, and P. J. Keely, 3D Collagen Alignment Limits Protrusions to Enhance Breast Cancer Cell Persistence, Biophys. J. **107**, 2546 (2014).

[6] A. J. Engler, S. Sen, H. L. Sweeney, and D. E. Discher, Matrix Elasticity Directs Stem Cell Lineage Specification, Cell **126**, 677 (2006).

[7] M. J. Paszek and V. M. Weaver, The Tension Mounts: Mechanics Meets Morphogenesis and Malignancy, J. Mammary Gland Biol. Neoplasia **9**, 325 (2004).

[8] P. P. Provenzano, K. W. Eliceiri, J. M. Campbell, D. R. Inman, J. G. White, and P. J. Keely, Collagen Reorganization at the Tumor-Stromal Interface Facilitates Local Invasion, BMC Med. **4**, 38 (2006).

[9] P. P. Provenzano, D. R. Inman, K. W. Eliceiri, and P. J. Keely, Matrix Density-Induced Mechanoregulation of Breast Cell Phenotype, Signaling and Gene Expression through a FAK–ERK Linkage, Oncogene **28**, 4326 (2009).

[10] X. Tang, P. Bajaj, R. Bashir, and T. A. Saif, How Far Cardiac Cells Can See Each Other Mechanically, Soft Matter **7**, 6151 (2011).

[11] D. Stopak and A. K. Harris, Connective Tissue Morphogenesis by Fibroblast Traction. I. Tissue Culture Observations, Dev. Biol. **90**, 383 (1982).

[12] T. Korff and H. G. Augustin, Tensional Forces in Fibrillar Extracellular Matrices Control Directional Capillary Sprouting, J. Cell Sci. **112**, 3249 (1999).

[13] R. K. Sawhney and J. Howard, Slow Local Movements of Collagen Fibers by Fibroblasts Drive the Rapid Global Self-Organization of Collagen Gels, J. Cell Biol. **157**, 1083 (2002).

[14] D. Vader, A. Kabla, D. Weitz, and L. Mahadevan, Strain-Induced Alignment in Collagen Gels, Plos One **4**, (2009).

[15] J. Notbohm, A. Lesman, P. Rosakis, D. A. Tirrell, and G. Ravichandran, Microbuckling of Fibrin Provides a Mechanism for Cell Mechanosensing, J. R. Soc. Interface **12**, 20150320 (2015).

[16] C. Storm, J. J. Pastore, F. C. MacKintosh, T. C. Lubensky, and P. A. Janmey, Nonlinear Elasticity in Biological Gels, Nature **435**, 191 (2005).

[17] A. M. Stein, D. A. Vader, D. A. Weitz, and L. M. Sander, The Micromechanics of Three-Dimensional Collagen-I Gels, Complexity **16**, 22 (2011).

[18] S. Motte and L. J. Kaufman, Strain Stiffening in Collagen I Networks, Biopolymers **99**, 35 (2013).

[19] N. A. Kurniawan, L. H. Wong, and R. Rajagopalan, Early Stiffening and Softening of Collagen: Interplay of Deformation Mechanisms in Biopolymer Networks, Biomacromolecules **13**, 691 (2012).

[20] P. L. Chandran and V. H. Barocas, Microstructural Mechanics of Collagen Gels in Confined Compression: Poroelasticity, Viscoelasticity, and Collapse, J. Biomech. Eng. **126**, 152 (2004).

[21] S. Münster, L. M. Jawerth, B. A. Leslie, J. I. Weitz, B. Fabry, and D. A. Weitz, Strain History Dependence of the Nonlinear Stress Response of Fibrin and Collagen Networks, Proc. Natl. Acad. Sci. USA **110**, 12197 (2013).

[22] S. Nam, J. Lee, D. G. Brownfield, and O. Chaudhuri, Viscoplasticity Enables Mechanical Remodeling of Matrix by Cells, Biophys. J. **111**, 2296 (2016).
[23] B. A. DiDonna and T. C. Lubensky, Nonaffine Correlations in Random Elastic Media, Phys. Rev. E **72**, 066619 (2005).
[24] D. A. Head, A. J. Levine, and F. C. MacKintosh, Distinct Regimes of Elastic Response and Deformation Modes of Cross-Linked Cytoskeletal and Semiflexible Polymer Networks, Phys. Rev. E **68**, 061907 (2003).
[25] D. A. Head, A. J. Levine, and F. C. MacKintosh, Mechanical Response of Semiflexible Networks to Localized Perturbations, Phys. Rev. E **72**, 061914 (2005).
[26] P. L. Chandran and V. H. Barocas, Affine versus Non-Affine Fibril Kinematics in Collagen Networks: Theoretical Studies of Network Behavior, J. Biomech. Eng. **128**, 259 (2006).
[27] H. Hatami-Marbini and R. C. Picu, Scaling of Nonaffine Deformation in Random Semiflexible Fiber Networks, Phys. Rev. E **77**, 062103 (2008).
[28] P. Grimmer and J. Notbohm, Displacement Propagation in Fibrous Networks Due to Local Contraction, J. Biomech. Eng. **140**, 041011 (2018).
[29] J. Feng, H. Levine, X. Mao, and L. M. Sander, Alignment and Nonlinear Elasticity in Biopolymer Gels, Phys. Rev. E **91**, 042710 (2015).
[30] A. J. Licup, S. Munster, A. Sharma, M. Sheinman, L. M. Jawerth, B. Fabry, D. A. Weitz, and F. C. MacKintosh, Stress Controls the Mechanics of Collagen Networks, Proc. Natl. Acad. Sci. USA **112**, 9573 (2015).
[31] M. Vahabi, A. Sharma, A. J. Licup, A. S. van Oosten, P. A. Galie, P. A. Janmey, and F. C. MacKintosh, Elasticity of Fibrous Networks under Uniaxial Prestress, Soft Matter **12**, 5050 (2016).
[32] A. S. van Oosten, M. Vahabi, A. J. Licup, A. Sharma, P. A. Galie, F. C. MacKintosh, and P. A. Janmey, Uncoupling Shear and Uniaxial Elastic Moduli of Semiflexible Biopolymer Networks: Compression-Softening and Stretch-Stiffening, Sci. Rep. **6**, 19270 (2016).
[33] K. L. Billiar and M. S. Sacks, A Method to Quantify the Fiber Kinematics of Planar Tissues under Biaxial Stretch, J. Biomech. **30**, 753 (1997).
[34] Q. Wen, A. Basu, J. P. Winer, A. Yodh, and P. A. Janmey, Local and Global Deformations in a Strain-Stiffening Fibrin Gel, New J. Phys. **9**, 428 (2007).
[35] J. Liu, G. H. Koenderink, K. E. Kasza, F. C. MacKintosh, and D. A. Weitz, Visualizing the Strain Field in Semiflexible Polymer Networks: Strain Fluctuations and Nonlinear Rheology of F-Actin Gels, Phys. Rev. Lett. **98**, 198304 (2007).
[36] T. T. Falzone and R. M. Robertson-Anderson, Active Entanglement-Tracking Microrheology Directly Couples Macromolecular Deformations to Nonlinear Microscale Force Response of Entangled Actin, ACS Macro Lett. **4**, 1194 (2015).
[37] T. M. Koch, S. Münster, N. Bonakdar, J. P. Butler, and B. Fabry, 3D Traction Forces in Cancer Cell Invasion, Plos One **7**, e33476 (2012).
[38] N. Gjorevski and C. M. Nelson, Mapping of Mechanical Strains and Stresses around Quiescent Engineered Three-Dimensional Epithelial Tissues, Biophys. J. **103**, 152 (2012).
[39] J. Steinwachs, C. Metzner, K. Skodzek, N. Lang, I. Thievessen, C. Mark, S. Munster, K. E. Aifantis, and B. Fabry, Three-Dimensional Force Microscopy of Cells in Biopolymer Networks, Nat. Methods (2015).
[40] J. Notbohm, A. Lesman, D. A. Tirrell, and G. Ravichandran, Quantifying Cell-Induced Matrix Deformation in Three Dimensions Based on Imaging Matrix Fibers, Integr. Biol. **7**, 1186 (2015).
[41] D. A. Stout, E. Bar-Kochba, J. B. Estrada, J. Toyjanova, H. Kesari, J. S. Reichner, and C. Franck, Mean Deformation Metrics for Quantifying 3D Cell-Matrix Interactions without Requiring Information about Matrix Material Properties, Proc. Natl. Acad. Sci. USA **113**, 2898 (2016).
[42] L. M. Owen, A. S. Adhikari, M. Patel, P. Grimmer, N. Leijnse, M. C. Kim, J. Notbohm, C. Franck, and A. R. Dunn, A Cytoskeletal Clutch Mediates Cellular Force Transmission in a Soft, 3D Extracellular Matrix, Mol. Biol. Cell **28**, 1959 (2017).

[43] B. Burkel and J. Notbohm, Mechanical Response of Collagen Networks to Nonuniform Microscale Loads, Soft Matter **13**, 5749 (2017).
[44] T. R. Matzelle, G. Geuskens, and N. Kruse, Elastic Properties of Poly(N-Isopropylacrylamide) and Poly(Acrylamide) Hydrogels Studied by Scanning Force Microscopy, Macromolecules **36**, 2926 (2003).
[45] B. Burkel, B. A. Morris, S. M. Ponik, K. M. Riching, K. W. Eliceiri, and P. J. Keely, Preparation of 3D Collagen Gels and Microchannels for the Study of 3D Interactions In Vivo, J. Vis. Exp. e53989 (2016).
[46] C. B. Raub, V. Suresh, T. Krasieva, J. Lyubovitsky, J. D. Mih, A. J. Putnam, B. J. Tromberg, and S. C. George, Noninvasive Assessment of Collagen Gel Microstructure and Mechanics Using Multiphoton Microscopy, Biophys. J. **92**, 2212 (2007).
[47] Y. Yang, L. M. Leone, and L. J. Kaufman, Elastic Moduli of Collagen Gels Can Be Predicted from Two-Dimensional Confocal Microscopy, Biophys. J. **97**, 2051 (2009).
[48] See Supplemental Material at [URL] for Five Supplemental Figures.
[49] D. N. Mashburn, H. E. Lynch, X. Ma, and M. S. Hutson, Enabling User-Guided Segmentation and Tracking of Surface-Labeled Cells in Time-Lapse Image Sets of Living Tissues, Cytometry A **81A**, 409 (n.d.).
[50] A. M. Stein, D. A. Vader, L. M. Jawerth, D. A. Weitz, and L. M. Sander, An Algorithm for Extracting the Network Geometry of Three□dimensional Collagen Gels, J. Microsc. **232**, 463 (2008).
[51] E. Bar-Kochba, J. Toyjanova, E. Andrews, K.-S. Kim, and C. Franck, A Fast Iterative Digital Volume Correlation Algorithm for Large Deformations, Exp. Mech. **55**, 261 (2015).
[52] J. P. Winer, S. Oake, and P. A. Janmey, Non-Linear Elasticity of Extracellular Matrices Enables Contractile Cells to Communicate Local Position and Orientation, Plos One **4**, e6382 (2009).
[53] M. S. Rudnicki, H. A. Cirka, M. Aghvami, E. A. Sander, Q. Wen, and K. L. Billiar, Nonlinear Strain Stiffening Is Not Sufficient to Explain How Far Cells Can Feel on Fibrous Protein Gels, Biophys. J. **105**, 11 (2013).
[54] S. B. Lindstrom, D. A. Vader, A. Kulachenko, and D. A. Weitz, Biopolymer Network Geometries: Characterization, Regeneration, and Elastic Properties, Phys. Rev. E **82**, 051905 (2010).
[55] S. B. Lindström, A. Kulachenko, L. M. Jawerth, and D. A. Vader, Finite-Strain, Finite-Size Mechanics of Rigidly Cross-Linked Biopolymer Networks, Soft Matter **9**, 7302 (2013).
[56] P. Ronceray, C. P. Broedersz, and M. Lenz, Fiber Networks Amplify Active Stress, Proc. Natl. Acad. Sci. USA **113**, 201514208 (2016).
[57] A. Basu, Q. Wen, X. Mao, T. C. Lubensky, P. A. Janmey, and A. G. Yodh, Nonaffine Displacements in Flexible Polymer Networks, Macromolecules **44**, 1671 (2011).
[58] J. Baselga, I. Hernandez-Fuentes, I. F. Pierola, and M. A. Llorente, Elastic Properties of Highly Crosslinked Polyacrylamide Gels, Macromolecules **20**, 3060 (1987).
[59] J. R. Tse and A. J. Engler, Preparation of Hydrogel Substrates with Tunable Mechanical Properties, Curr. Protoc. Cell Biol. 10 (2010).
[60] D. L. Holmes and N. C. Stellwagen, Estimation of Polyacrylamide Gel Pore Size from Ferguson Plots of Linear DNA Fragments. II. Comparison of Gels with Different Crosslinker Concentrations, Added Agarose and Added Linear Polyacrylamide, Electrophoresis **12**, 612 (1991).
[61] H. Hatami-Marbini and R. C. Picu, Heterogeneous Long-Range Correlated Deformation of Semiflexible Random Fiber Networks, Phys. Rev. E **80**, 046703 (2009).
[62] D. Velegol and F. Lanni, Cell Traction Forces on Soft Biomaterials. I. Microrheology of Type I Collagen Gels, Biophys. J. **81**, 1786 (2001).
[63] M. A. Kotlarchyk, S. G. Shreim, M. B. Alvarez-Elizondo, L. C. Estrada, R. Singh, L. Valdevit, E. Kniazeva, E. Gratton, A. J. Putnam, and E. L. Botvinick, Concentration Independent Modulation of Local Micromechanics in a Fibrin Gel, Plos One **6**, e20201 (2011).
[64] M. Shayegan and N. R. Forde, Microrheological Characterization of Collagen Systems: From Molecular Solutions to Fibrillar Gels, Plos One **8**, e70590 (2013).

[65] C. A. Jones, M. Cibula, J. Feng, E. A. Krnacik, D. H. McIntyre, H. Levine, and B. Sun, Micromechanics of Cellularized Biopolymer Networks, Proc. Natl. Acad. Sci. USA **112**, E5117 (2015).
[66] R. C. Arevalo, P. Kumar, J. S. Urbach, and D. L. Blair, Stress Heterogeneities in Sheared Type-I Collagen Networks Revealed by Boundary Stress Microscopy, Plos One **10**, e0118021 (2015).
[67] F. Tang, C. Barbacioru, S. Bao, C. Lee, E. Nordman, X. Wang, K. Lao, and M. A. Surani, Tracing the Derivation of Embryonic Stem Cells from the Inner Cell Mass by Single-Cell RNA-Seq Analysis, Cell Stem Cell **6**, 468 (2010).
[68] A. K. Shalek, R. Satija, X. Adiconis, R. S. Gertner, J. T. Gaublomme, R. Raychowdhury, S. Schwartz, N. Yosef, C. Malboeuf, and D. Lu, Single-Cell Transcriptomics Reveals Bimodality in Expression and Splicing in Immune Cells, Nature **498**, 236 (2013).
[69] A. P. Patel, I. Tirosh, J. J. Trombetta, A. K. Shalek, S. M. Gillespie, H. Wakimoto, D. P. Cahill, B. V. Nahed, W. T. Curry, and R. L. Martuza, Single-Cell RNA-Seq Highlights Intratumoral Heterogeneity in Primary Glioblastoma, Science **344**, 1396 (2014).
[70] A. Zeisel, A. B. Muñoz-Manchado, S. Codeluppi, P. Lönnerberg, G. La Manno, A. Juréus, S. Marques, H. Munguba, L. He, and C. Betsholtz, Cell Types in the Mouse Cortex and Hippocampus Revealed by Single-Cell RNA-Seq, Science **347**, 1138 (2015).
[71] F. Beroz, L. M. Jawerth, S. Münster, D. A. Weitz, C. P. Broedersz, and N. S. Wingreen, Physical Limits to Biomechanical Sensing in Disordered Fibre Networks, Nat. Commun. **8**, 16096 (2017).